Earth and Planetary Science Letters 349–350 (2012) 198–208

Contents lists available at SciVerse ScienceDirect

Earth and Planetary Science Letters

journal homepage: www.elsevier.com/locate/epsl

The primitive nature of large low shear-wave velocity provinces

Frédéric Deschamps [a,b,*], Laura Cobden [c], Paul J. Tackley [b]

[a] Institute of Earth Sciences, Academia Sinica, 128 Academia Road Sec. 2, Nangang, Taipei 11529, Taiwan
[b] Institute of Geophysics, Swiss Federal Institute of Technology Zurich, Sonnegstrasse 5, Zurich 8092, Switzerland
[c] Institut für Geophysik, Westfälische Wilhelms Universität Münster, Corrensstrasse 24, Münster 48149, Germany

ARTICLE INFO

Article history:
Received 6 December 2011
Received in revised form
27 June 2012
Accepted 7 July 2012
Editor: T. Spohn

Keywords:
mantle structure
mantle dynamics
low shear-wave velocity provinces

ABSTRACT

The lowermost (> 2400 km) Earth's mantle mapped by seismic tomography is strongly heterogeneous, the most striking feature being two large regions where shear-wave velocity drops by a few percent compared to averaged mantle. Additional seismic observations indicate that these structures cannot result from purely thermal effects. Compositional anomalies are required to fully explain seismic observations, but their exact nature is still debated. Here, we show that low shear-wave velocity provinces unlikely consist of recycled oceanic crust (MORB). We calculated seismic sensitivity to high-pressure MORB, and found that in the lowermost mantle shear-wave velocity increases with increasing fraction of MORB. Therefore, unless they are heated up to unrealistic temperatures, high-pressure MORB would induce high shear-wave velocity, in contradiction with the observations. Instead, material enriched in iron by ~3.0% and in (Mg,Fe)-perovskite by ~20% compared to regular mantle provides a good explanation for the low shear-wave velocity provinces and for the high bulk-sound velocities observed in the same areas. In addition, several geochemical and geodynamical arguments support a primitive origin for this material. Low shear-wave velocity provinces may thus consist of reservoirs of primitive material that have differentiated early in the Earth's history.

1. Introduction

The Earth's lowermost (> 2400 km) mantle structure mapped from seismic tomography is dominated by two large low shear-wave provinces (LLVSP) about 5000 km wide and located beneath the Pacific and Africa (e.g., Su et al., 1994; Li and Romanowicz, 1996). LLVSP were first interpreted as hot, buoyant superplumes, but several seismological observations invalidated this hypothesis. The depth variation of the laterally averaged seismic ratios (van der Hilst and Kárason, 1999; Masters et al., 2000), the strong lateral dispersion of these ratios at a given depth (Deschamps and Trampert, 2003), the anti-correlation between bulk-sound and shear-wave velocity anomalies (Ishii and Tromp, 1999; Masters et al., 2000; Trampert et al., 2004), and the decorrelation between the shear-wave velocity and density anomalies mapped by normal mode tomography (Ishii and Tromp, 1999; Trampert et al., 2004) cannot be explained by variations of temperature only. Additional geophysical observations, independent from seismology, suggest that LLVSP have remained stable since at least 200 Ma. First, reconstructed positions of large igneous provinces are systematically located above LLVSP (Torsvik et al., 2008). Second, a recent mass redistribution at the bottom of the mantle, leading to the actual LLVSP, would induce a true polar wander significantly larger than the observed one (Dziewonski et al., 2010). These observations further invalidate a purely thermal nature of LLVSP, since hot superplumes would be dynamically unstable in the long term. By contrast, it is possible to build models of thermo-chemical convection in which basal reservoirs of dense material remain stable over periods comparable to the age of the Earth (next paragraph). Geophysical observations and geodynamic models thus clearly indicate that LLVSP result from the combination of thermal and chemical heterogeneities. The nature of these chemical anomalies is however still debated, and two end-members hypotheses, the recycling of oceanic crust (MORB) and the survival of reservoir(s) of primitive material, are usually advocated.

Dynamically, both the segregation of MORB and the survival of dense material are feasible. Numerical models of thermal convection showed that cold downwellings can cross the endothermic phase transition at 660-km depth (e.g., Machetel and Weber, 1991), and early models of thermo-chemical convection indicated that recycled crust may be segregated at the bottom of the mantle (Christensen and Hofmann, 1994). More recent models pointed out that the shape and stability of the reservoirs of MORB depend on the assumed composition of MORB in main oxides (Nakagawa et al., 2010). Meanwhile, experimental (Davaille, 1999; Le Bars and Davaille, 2004) and numerical (Tackley, 2002; McNamara and

* Corresponding author at: Institute of Earth Sciences, Academia Sinica, 128 Academia Road Section 2, Nangang, Taipei 11529, Taiwan. Tel.: +886 2 27839910.
E-mail address: frederic@earth.sinica.edu.tw (F. Deschamps).

0012-821X/$ - see front matter © 2012 Elsevier B.V. All rights reserved.
http://dx.doi.org/10.1016/j.epsl.2012.07.012

Zhong, 2004; Tan and Gurnis, 2007; Deschamps and Tackley, 2008, 2009) models of thermo-chemical convection including an initial layer of dense material showed that reservoirs of dense material can be maintained at the bottom of the system. The shape and stability of these reservoirs depend on several parameters, including the chemical density contrast between the dense and regular materials (Davaille, 1999; Le Bars and Davaille, 2004; McNamara and Zhong, 2004; Deschamps and Tackley, 2009), and the thermal viscosity contrast (Deschamps and Tackley, 2008). The combination of a moderate (80–100 kg/m^3) chemical density contrast and a large (10^4 and more) thermal viscosity contrast allows pools of dense material to be maintained for periods of time comparable to the age of the Earth. Furthermore, the endothermic phase transition at 660-km adds some negative buoyancy, which prevents the dense material from massively entering the upper mantle (Le Bars and Davaille, 2004; Deschamps and Tackley, 2009, van Summeren et al., 2010).

Recycled MORB and primitive material are both denser than average mantle, but differ in their seismic signatures. The details of these signatures may thus be used to assess the nature of LLVSP. Inferring seismic signatures requires the knowledge of appropriate seismic sensitivities to the temperature and chemical components that contribute in the mantle aggregate. This, in turn, requires careful modeling of the equation of state of the mantle aggregate. One difficulty when modeling the mantle aggregate equation of state is to account for uncertainties in the thermodynamic and thermo-elastic properties of mantle minerals. This difficulty can however be addressed by performing Monte-Carlo searches, resulting in full probability density functions of the seismic sensitivities (Trampert et al., 2001; Deschamps and Trampert, 2003). So far, no sensitivities were calculated for MORB. Here, we have calculated a set of seismic sensitivities, including MORB sensitivities, using a recent mineral physics dataset (Stixrude and Lithgow-Bertelloni, 2011). We have then calculated synthetic seismic velocities induced by both high pressure MORB and materials enriched in iron and silicate, and compare them with seismic tomographic features. We also derived seismic velocity anomalies from thermo-chemical distributions predicted by recent numerical models of convection (Deschamps et al., 2011). Our calculations suggest that LLVSP are better explained by material enriched in iron and silicate than by recycled MORB.

2. Seismic sensitivities

Linking thermo-chemical anomalies to seismic velocity and density anomalies requires knowledge of seismic sensitivities, which can be calculated from appropriate equation of state modeling and mineral physics data. Here, we calculated sensitivities of shear-wave velocity (V_S), bulk-sound velocity (V_Φ), and density (ρ) to temperature, MORB, iron (partitioned in FeO and $FeSiO_3$), perovskite (meaning $MgSiO_3$ plus $FeSiO_3$), and post-perovskite by combining a recent equation of state modeling (Cobden et al., 2012) and a self-consistent mineral physics dataset (Stixrude and Lithgow-Bertelloni, 2011). Our approach accounts for various sources of uncertainties in thermo-elastic data, and therefore allows the determination of full distribution of these sensitivities.

2.1. Method

Seismic sensitivities are defined as the partial derivatives $\partial \ln V_S/\partial x$, $\partial \ln V_\Phi/\partial x$, and $\partial \ln \rho/\partial x$, where x is either the temperature or the volume fraction of a chemical component, and are calculated as the finite difference between the seismic properties of a reference mineralogical model and those of a perturbed model. The reference model has a temperature and mineralogy chosen at random within very broad ranges (Supplementary Tables S1–S3). In the perturbed model, we alter the composition or temperature by a fraction of a percent relative to the reference model. For calculating the sensitivity of seismic properties to temperature changes the chemical composition is the same in the reference and perturbed models, but the temperature may vary by up to 1 K. In this case,

$$\frac{\partial \ln V}{\partial T} = \frac{1}{V_{\rm ref}} \frac{(V_{\rm per} - V_{\rm ref})}{(T_{\rm per} - T_{\rm ref})}, \quad (1)$$

where V refers to V_Φ, V_S or ρ, and subscripts per and ref refer to the perturbed and reference models, respectively. For chemical changes, T is kept fixed and the volume fraction of the chemical component of interest X (e.g., MORB, global iron, SiO_2, perovskite) is changed by up to 0.1% between the reference and perturbed model. Where X is a mineral assemblage rather than a single mineral, the relative proportions of the constituent minerals of X are kept constant. Likewise, while the volume of the residual chemical component (i.e. the non-MORB component) changes by up to 0.1%, the ratios of the minerals within that component are the same for the reference and perturbed models. In this case,

$$\frac{\partial \ln V}{\partial X} = \frac{1}{V_{\rm ref}} \frac{(V_{\rm per} - V_{\rm ref})}{(\vartheta_{\rm per} - \vartheta_{\rm ref})}, \quad (2)$$

where ϑ is the volume fraction of chemical component X in the bulk mineralogical assemblage. Differences between the reference and perturbed models are summarised in Supplementary Table S4. We performed additional calculations in which temperature and chemical perturbations, dT and dϑ, are allowed to vary by much larger amounts, up to 2000 K and 20% (100% for MORB), and found that the sensitivities remain unchanged, both in average value and distribution. Our sensitivities therefore do not depend on the choice of dT and dϑ.

The values of seismic derivatives depend not only on the T or X with respect to which they are calculated, but will also change according to the temperature and composition of the reference model (Trampert et al., 2001) and, in the case where X is an assemblage of minerals, according to the volume fractions of the different minerals within X. Because we do not know the precise reference (average) thermo-chemical structure of the mantle (Cobden et al., 2009), we calculated seismic derivatives for 100,000 reference and perturbed models, with each reference model having a different and randomly selected temperature and composition, and, where relevant, each chemical component X having a different composition. Such a Monte-Carlo procedure, first employed by Trampert et al. (2001), therefore turns the unknown thermo-chemical reference model into uncertainties. In our case, it produces a collection of 100,000 measurements of $d\ln V_\Phi$, $d\ln V_S$ and $d\ln\rho$, which we can analyse statistically to place robust constraints on the likelihood of different thermo-chemical structures existing in the mantle. The model space of mineralogical composition we need to explore is huge. To test the stability of our approach, i.e. that we properly sample the model space of oxide composition, we analysed distributions of sensitivities obtained with the number of samples N varying between 100 and 200,000. We found that the average in distributions vary very little with N, by 5% or less. More importantly, for $N \geq 10{,}000$, the full distributions of seismic sensitivities do not change significantly, as indicated by frequency histograms in Figure S1. Seismic sensitivity distributions obtained by sampling the composition model space with 100,000 realisations, as we do in this study, are therefore statistiscally relevant.

We calculated $\partial \ln V/\partial X$ for changes in the volume fractions of MORB, perovskite, iron, SiO_2, and post-perovskite. Perovskite changes are defined as changes in the total volume fraction of

Table 1
Mineralogy ranges for MORB component when calculating the seismic sensitivities to MORB. Ranges are based on several published MORB compositions (Hofmann, 1998; Irifune and Ringwood, 1993; Ono et al., 2001, 2005; Hirose et al., 2005; Ricard et al., 2005; Perrillat et al., 2006; Ricolleau et al., 2010). Unit is volume fraction.

Mineral	Min	Max
$MgSiO_3$	0.210	0.281
$FeSiO_3$	0.120	0.190
$CaSiO_3$	0.238	0.286
Al_2SiO_3	0.167	0.179
SiO_2	Fixed as 1.0 minus the sum of above components, restricted to the range 12–22%	

$MgSiO_3$ plus $FeSiO_3$, whilst iron (Fe) changes refer to changes in the volume fractions of FeO plus $FeSiO_3$. SiO_2 changes refer to changes in the volume fraction of the free-SiO_2 phase only. The petrologically-observed chemical composition of MORB is highly variable, and therefore we allow the composition of the MORB component in our models to vary within ranges that accomodate a large number of observations (Table 1, and references therein).

Seismic derivatives are calculated every 100 km between 700 and 2900 km depth, and using the mineral elastic parameters of a recent dataset (Stixrude and Lithgow-Bertelloni, 2011) together with the equation of state in (Stixrude and Lithgow-Bertelloni, 2005). This is a third-order finite strain Birch–Murnaghan equation of state, coupled with a Mie–Grüneisen thermal pressure correction for the temperature.

To convert from thermo-chemical structure to seismic properties, we first calculate the bulk modulus K, shear modulus G, and density ρ for each mineral present at the pressure and temperature of interest. Then, we compute the overall bulk and shear moduli of the full mineral assemblage by taking the Voigt–Reuss–Hill average of the K's and G's of the constituent minerals. The bulk density is taken to be the average of the densities of all of the minerals present, weighted according to their volume fractions. Seismic velocities V_S and V_Φ are calculated using these averaged values for K, G and ρ. Note that velocities are not corrected for anelasticity since the effects of anelasticity have been shown to be negligible in the lower mantle (Brodholt et al., 2007), where the effect of high pressure dominates over high temperature.

Mineral physics uncertainties are taken into account by allowing the elastic parameters of each mineral to adopt a value chosen at random from within the uncertainty bars published in Stixrude and Lithgow-Bertelloni (2011). Elastic parameters for each mineral do not change between a reference and its associated perturbed model, but rather vary between the 100,000 reference–perturbed model pairs. We find that the seismic effect of the mineral physics uncertainties published in Stixrude and Lithgow-Bertelloni (2011) is much smaller than the effect due to changes in the temperature and composition of the reference model or of X.

We include seven end-member mineralogical phases in our calculations: $MgSiO_3$ perovskite, $FeSiO_3$ perovskite, FeO wüstite, MgO periclase, Al_2O_3 perovskite, $CaSiO_3$ perovskite, and SiO_2 seifertite. Below 2200 km, we run two sets of simulations: one with only these seven minerals, and one in which $MgSiO_3$, $FeSiO_3$ and Al_2O_3 may also be present as post-perovskite. For clarity in the figures we here show only the seismic derivatives of the 100,000 models not containing post-perovskite. However, we discuss the effect of including post-perovskite (which is generally small) in Section 4. For computational efficiency, and because phase changes in free SiO_2 at high pressure are poorly constrained, we assume that SiO_2 is present as the seifertite phase throughout the lower mantle. According to our elastic parameter dataset, the elastic properties of the various lower mantle SiO_2 polymorphs are similar, and the seismic sensitivity to free SiO_2 is very small, so this simplification does not change our results.

We chose to impose a mineralogical composition rather than to calculate it from Gibbs free energy minimization because such minimization would require an exaggerated computational time. However, it is important to note that our range of mineralogical compositions encompasses feasible compositions for the lower mantle to which we added some error bars *a priori*, and that we varied the average temperature within a possible range for the lower mantle. Doing so, we implicitly explore the model space of mineralogical composition, thus compensating the fact that we do not solve for the exact composition. We have also checked (Section 5) that material enriched in iron and perovskite, which we find to explain LLVSP better than MORB, is stable at lower mantle temperature and pressure, and can be obtained by minimization of Gibbs free energy. The advantage of our approach is that we obtain full distributions of seismic sensitivities, which can further be used to calculate full distributions of seismic velocity anomalies, allowing quantitative comparison against seismic tomography.

2.2. Results

Fig. 1 displays seismic sensitivities to MORB. A remarkable feature is that the sensitivities of both V_S and V_Φ are mostly positive (i.e. V_S and V_Φ increase with increasing MORB fraction) throughout the lower mantle. In the lowermost mantle, the sensitivities of V_S and V_Φ are positive with a confidence level of 0.75 and 0.60, respectively. This observation has two important consequences. First, to induce V_S-anomalies around -2.0%, a typical value for LLVSP (Su et al., 1994; Li and Romanowicz, 1996; Ishii and Tromp, 1999; Masters et al., 2000; Trampert et al., 2004), high-pressure MORB should be very hot. Second, V_S- and V_Φ-anomalies should be correlated, in contradiction with seismic tomography (Masters et al., 2000; Trampert et al., 2004). We further quantify these effects in Section 3.

Sensitivities to temperature, iron, and perovskite (Supplementary Figures S2–S4) are comparable to those calculated in previous studies (Deschamps and Trampert, 2003; Trampert et al., 2004), with slight changes in amplitude. In particular, V_S strongly decreases with increasing fraction of iron, whereas V_Φ increases with increasing fraction of perovskite. Material enriched in iron and perovskite would therefore appear slower than pyrolitic mantle in V_S, and faster in V_Φ. Supplementary Figure S5 shows the sensitivity to free SiO_2, which may be in excess in the lowermost mantle (Javoy et al., 2010). The sensitivity of V_S to SiO_2 is small and goes to zero in the lowermost mantle, whereas the sensitivity of V_Φ to SiO_2 is positive throughout the lower mantle. The influence of SiO_2 should thus be close to that of perovskite (compare Supplementary Figs. S4 and S5). A notable difference, compared to perovskite, is that the sensitivity of V_S to SiO_2 is slightly larger than that of V_S to perovskite. Therefore, if excess in perovskite is replaced by excess in free SiO_2, a larger fraction of iron and/or larger temperatures may be required to

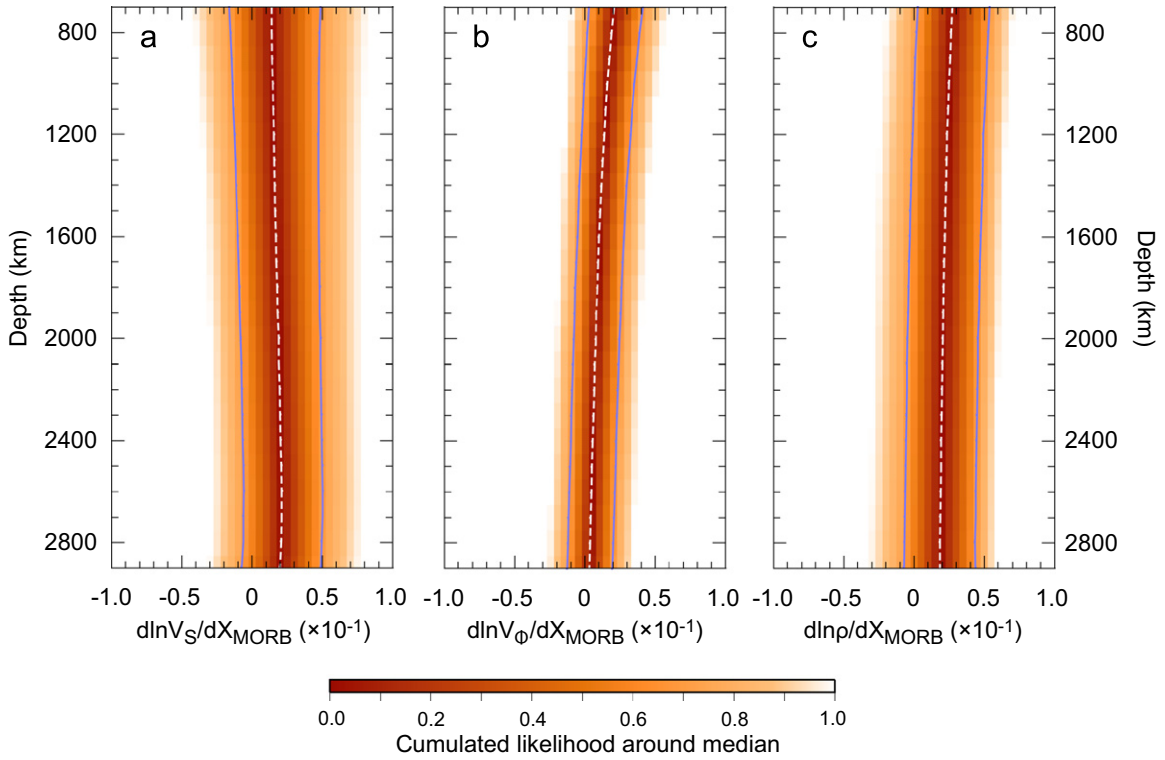

Fig. 1. Sensitivities of shear-wave velocity (left), bulk-sound velocity (middle), and density (right) to the volume fraction of MORB as a function of depth. The color code indicates the cumulated likelihood around the median value. On each plot, the white dashed line indicates the median value (i.e., 50% of the explored sensitivities lie on each side of this line), and the blue curves represent the 0.15 and 0.85 quartiles (i.e., 70% of the explored sensitivities lie within the area bounded by these curves).

induce low (up to −2.0%) shear-wave velocity anomalies. Finally, Supplementary Figure S6 plots the sensitivities to post-perovskite where applicable (i.e., in our calculations, at depths larger than 2200 km). These sensitivities indicate that an increase in post-perovskite would result in an increase of V_S, but would leave V_Φ unchanged.

3. Synthetic seismic velocity anomalies

Using the sensitivities in Fig. 1 and Supplementary Figs. S2–S4, we calculated synthetic relative shear-wave (dlnV_S) and bulk-sound (dlnV_Φ) seismic velocity anomalies induced by a combination of temperature anomalies and compositional anomalies of different nature. We considered two independent sources of chemical heterogeneity, recycled MORB (with dX_{MORB}=1 in Eq. (3) below) and material enriched both in iron (partitioned in FeO and $FeSiO_3$) and silicate (parameterized as an enrichment in Fe- and Mg-perovskite, hereafter referred to as perovskite). In the latter case, we assumed enrichment (compared to horizontal average) in iron and perovskite by 1.5% and 9.0%, respectively, as suggested by probabilistic tomography (Trampert et al., 2004). Thermo-chemical models from updated probabilistic tomography (Mosca et al., 2012), which also accounts for the presence of post-perovskite, confirm such excess in iron and perovskite, with somewhat larger (up to 3.0–4.0%) iron excess. Synthetic anomalies are then simply writen as the sum of thermal and compositional anomalies weighted by appropriate sensitivities. For each of the two sources of chemical anomalies we considered, the relative seismic anomalies are calculated by

$$\mathrm{dln}V = \frac{\partial \mathrm{ln}V}{\partial T} dT + \frac{\partial \mathrm{ln}V}{\partial X_{MORB}} \mathrm{d}X_{\mathrm{MORB}}, \quad (3)$$

and

$$\mathrm{dln}V = \frac{\partial \mathrm{ln}V}{\partial T} \mathrm{d}T + \frac{\partial \mathrm{ln}V}{\partial X_{Pv}} dX_{Pv} + \frac{\partial \mathrm{ln}V}{\partial X_{\mathrm{Fe}}} \mathrm{d}X_{\mathrm{Fe}}, \quad (4)$$

where V stands for V_Φ, V_S or ρ, and X_{MORB}, X_{Pv}, and X_{Fe} are the volume fractions of MORB, perovskite, and iron. One may point out that because MORB is naturally enriched in iron, increasing the volume fraction of MORB fraction or the volume fraction of global iron fraction should lead to similar results. A major difference, however, is that MORB does not include periclase (MgO) and ferropericlase (FeO). Because the effects of iron on shear-wave velocity are more pronounced in periclase (Kung et al., 2002) than in Mg-perovskite (Kiefer et al., 2002), a global increase in the global volume fraction of iron is unlikely to be equivalent to an increase of the volume fraction of MORB.

3.1. Frequency histograms and likelihoods

Since we calculated full distributions of seismic sensitivities, we could determine full distributions of seismic velocities and density anomalies by sampling the seismic sensitivities according to their own distribution. Distributions give access to several statistical quantities, including probabilities that dln$V$ lie within a specific range. Fig. 2 shows frequency histograms of dlnV_S and dlnV_Φ induced either by high pressure MORB or by material enriched in iron and perovskite in the layer 2700–2880 km (corresponding to the lowermost layer of tomographic model SB10L18), and Fig. 3a plots the likelihoods that dlnV_S and dlnV_Φ are within prescribed ranges as a function of the temperature anomaly. Note that the distributions for MORB are broader, due to the uncertainties in MORB composition in the main oxides (Table 1 and references therein).

Figs. 2 and 3a clearly show that for a temperature excess in the range 400–700 K, a combined enrichment in iron and perovskite is

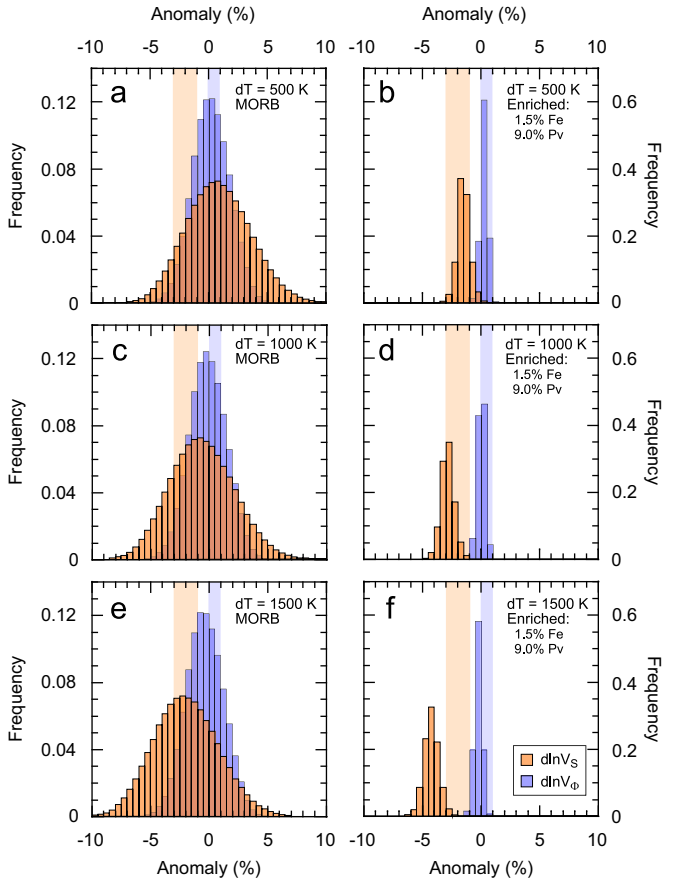

Fig. 2. Frequency histograms of shear-wave velocity (orange) and bulk sound velocity (blue) anomalies for high pressure MORB (left column), and for a material enriched (compared to the horizontally average mantle) in iron and (Mg,Fe)-perovskite by 1.5% and 9.0%, respectively (right column). Three values of the temperature anomaly (compared to average mantle) are considered, from top to bottom dT=500 K, dT=1000 K, and dT=1500 K. Shaded vertical bands indicate typical values for LLVSP observed from seismic tomography. Calculations are made in the layer 2700–2880 km, corresponding to the lowermost layer of tomographic model SB10L18 (Masters et al., 2000).

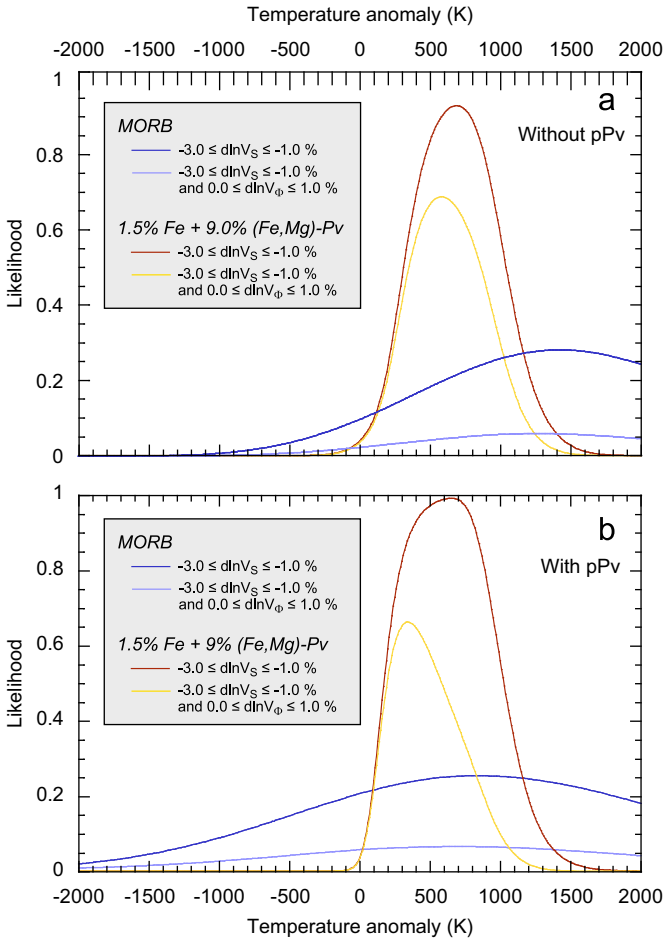

Fig. 3. Likelihoods of relative seismic anomalies as a function of temperature anomalies without (plot a) and with (plot b) post-perovskite in the lowermost mantle. In both cases, two types of chemical heterogeneities are considered, MORB with dX_{MORB}=1 in Eq. (3) (blue curves), and material enriched (compared to horizontally average mantle) in iron and (Mg,Fe)-perovskite by 1.5% and 9.0%, respectively (orange curves). For each chemical source, we represent the likelihood that shear-wave velocity anomaly (dlnV_S) is between −3.0 and −1.0% (dark curves), and the combined likelihood for shear-wave and bulk-sound (dlnV_Φ) velocities to lie between −3.0% and −1.0% and 0 and 1.0%, respectively (light curves). Calculations are made in the layer 2700–2880 km, corresponding to the lowermost layer of tomographic model SB10L18 (Masters et al., 2000).

more likely to explain LLVSP than recycled MORB. For a temperature excess of 500 K, frequency histograms of the dlnV_S and dlnV_Φ induced by enriched material have median values equal to −1.6% and 0.3% (Fig. 2), respectively, which are typical values observed by classical (Masters et al., 2000) and probabilistic (Trampert et al., 2004) tomography. The likelihood of simultaneously finding dlnV_S between −3.0 and −1.0% and dlnV_Φ between 0 and 1.0% is high (>0.6) in the range of temperature excess 400–700 K (Fig. 3a). Median anomalies decrease with increasing excess temperature, and for $\Delta T > 1000$ K the median dlnV_Φ is negative, in contradiction with seismic tomography (Ishii and Tromp, 1999; Masters et al., 2000; Trampert et al., 2004). By contrast, MORB with an excess temperature in the range 500–1000 K induces positive dlnV_S (Fig. 2), and therefore does not explain the observed dlnV_S. To induce dlnV_S in agreement with observed values, around −2.0%, the excess temperature in MORB should reach 1500 K. For such temperature excess, the likelihood that $-3.0\% \le \mathrm{dln}V_S \le -1.0\%$ peaks at 0.3, but it drops to less than 0.1 if one also requires that $0.0 \le \mathrm{dln}V_\Phi \le 1.0\%$ (Fig. 3a). Note that individually an excess in iron or an excess in perovskite is unlikely to fully explain seismic tomography. Sensitivities of both V_S and V_Φ to iron are negative (Supplementary Figure S3), i.e. an excess in iron alone would result in negative anomalies in both V_S and V_Φ. Sensitivity of V_Φ to perovskite is positive throughout the lower mantle (thus inducing positive V_Φ-anomalies), but sensitivity of V_S to perovskite spreads around zero (Supplementary Figure S4), implying that V_S-anomalies around −2.0% would require a large (>1000 K) temperature excess.

The main conclusion of this series of calculations is that recycled MORB are unlikely to induce dlnV_S observed in LLVSP, unless they are heated at 1500 K above the average mantle temperature (in which case the likelihood of explaining both dlnV_S and dlnV_Φ remains low). There is no direct measurement of the excess temperature in the deep mantle, but a good approximation can be deduced from the excess temperature in hotspots, keeping in mind that several effects including internal heating, which induces sub-adiabatic temperature profiles (Parmentier et al. 1994), adiabatic cooling being greater at higher temperature (Albers and Christensen, 1996; Bunge, 2005; Leng and Zhong, 2008), lateral diffusion (Mittelstaedt and Tackley, 2005) viscous dissipation, and the presence of chemical reservoirs at the bottom of the mantle (Farnetani, 1997) may strongly reduce the

temperature excess in the plume. Petrology indicates a temperature excess in plumes of 250–300 K (Campbell and Griffiths, 1990), which, for a compositional excess density between 2.0% and 5.0%, implies temperature anomalies at the foot of the plume between 600 and 800 K (Farnetani, 1997). The excess temperature in the lowermost mantle may also be estimated from the superadiabatic temperature jump at the bottom ΔT_{bot}, assuming that the total lateral temperature difference at the bottom of the mantle scales as the temperature jump across the bottom thermal boundary layer. Most recent estimates of ΔT_{bot} are around 1500 K (Tackley, in press), leading to lateral anomalies of temperature (relative to average) around ± 750 K. Both estimates are consistent with a material enriched iron and perovskite (Fig. 3), but are about half the temperature excess required for MORB to induce a $d\ln V_S$ around -2.0%.

3.2. Anomalies reconstructed from geodynamic modeling

As an additional test, we have calculated the seismic velocity anomalies induced by the distribution of temperature and composition predicted by thermo-chemical convection. Here, we used a recent 3D-Cartesian model (Deschamps et al., 2011) represented in Fig. 4. This model was obtained with StagYY (Tackley, 2008), which solves the conservation equations of mass, momentum, energy, and composition for an anelastic, compressible fluid with infinite Prandtl number. The effective Rayleigh number is around 3.0×10^6, which is consistent with expected values of the Rayleigh number for the Earth's mantle. The compositional field is modeled by a collection of tracer particles of two types, regular and dense. At each location, the composition is calculated by the concentration C of dense particles, which varies between 0 and 1. The density contrast between the dense and regular material is controlled by the buoyancy ratio, which is here fixed to 0.22 (equivalent to a chemical density contrast of 90 kg/m^3). The nature of the dense material is however not prescribed *a priori*. Viscosity is strongly temperature-dependent, with logarithmic viscosity ratio of 10^6 leading to a top to bottom viscosity ratio of 4000, and a viscosity increase at 660-km depth of factor 30. The Clapeyron slope of the 660-km phase transition is fixed to -2.5 MPa/K. For this set of parameters, large reservoirs of dense material are generated at the bottom of the model (Fig. 4, plots a and b). These structures remain stable during a period of time larger than the age of the Earth, and they induce strong chemical density anomalies, as indicated by spectral heterogeneity maps (representing Fourier spectra as a function of depth) of chemical density anomalies (Fig. 4, plot e) and profiles of the RMS in chemical density anomalies (Fig. 4, plot f). Strong temperature anomalies, including cold downwellings, are also generated (Fig. 4, plots c and d). Note that the dense reservoirs are hotter than average. Together with the cold downwellings, this induces substantial thermal density anomalies in the lowermost part of the system (Fig. 4, plots g and h).

Again, we calculated relative anomalies of shear-wave and bulk sound velocities assuming two different possible natures for the compositional anomalies: high-pressure MORB (following Eq. (3)), and material enriched in iron and perovskite (following Eq. (4)). In the case of MORB, the composition in each cell varies between regular mantle ($C=0$) and 100% MORB ($C=1$). In the case

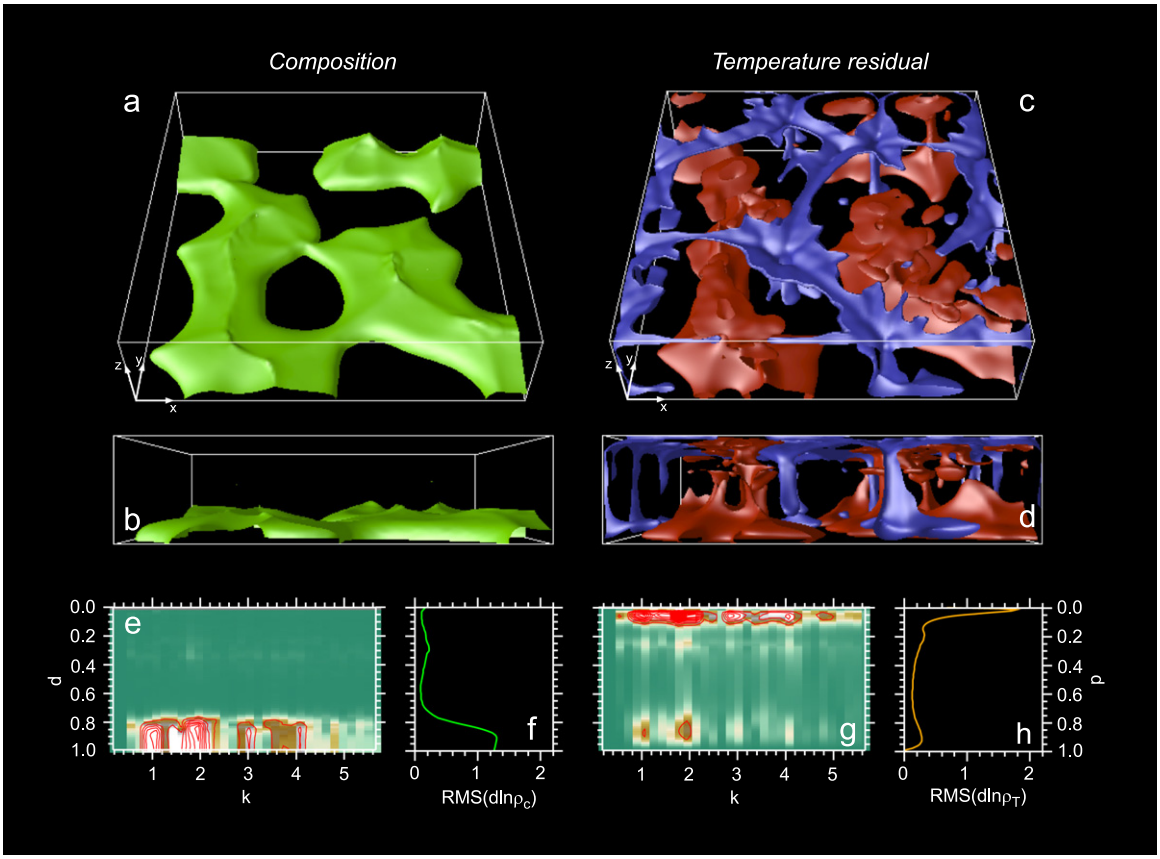

Fig. 4. Thermo-chemical distributions used as input for the calculation of seismic velocity anomalies. (a and b) Isosurface of the compositional field, with value $C=0.5$. (c and d) Isosurfaces of the residual non-dimensional temperature (with respect to the mean temperature), with values $\delta T=-0.125$ (blue) and $\delta T=0.125$ (red). Taking $\Delta T=2500$ K as characteristic temperature scale, this leads to temperature anomalies of ± 312.5 K. (e) Spectral heterogeneity maps (SHM) of the chemical density anomalies, dln ρ_C. (f) Profile of the RMS of dln ρ_C. (g) SHMs of the thermal density anomalies, dln ρ_T. (h) Profile of the RMS of dln ρ_T. Details of the numerical modeling can be found in Deschamps et al. (2011).

of enriched material, the composition in each cell varies between regular mantle ($C=0$), and material enriched in iron and perovskite by 3.0% and 18% compared to the regular mantle ($C=1$). At the bottom of the system, where compositional reservoirs are present, this leads to anomalies relative to horizontally averaged mantle of $\pm 1.5\%$ in iron and $\pm 9.0\%$ in perovskite, consistent with estimates from probabilistic tomography (Trampert et al., 2004). Note that since the sensitivities we calculated are only defined with lower mantle minerals, the seismic anomalies we calculated are not relevant for the upper mantle. For convenience, we however assumed that lower mantle minerals are also stable in the upper mantle, and we extrapolated our sensitivities upward to the surface, and represented synthetic seismic anomalies over the entire system. Since our main focus here is the lowermost mantle, this flaw does not alter our main conclusions. Furthermore, compositional anomalies are very small in the upper mantle (Fig. 4, panels a–b and e–f), and thus, they do not significantly contribute to the reconstructed seismic velocity anomalies, which are dominated by thermal anomalies. In experiments of thermo-chemical convection, temperature is non-dimensional. The determination of the thermal contribution to the seismic anomalies therefore requires rescaling the thermal distribution with the super-adiabatic temperature jump. Here, we varied this jump in the range 2000–3000 K to account for uncertainties in its real value. For comparison with seismic tomography, we degraded the resolution of the synthetic seismic anomalies. First, we vertically averaged these anomalies according to the vertical parameterization of SB10L18 (Masters et al., 2000). In each layer, we then applied a 2D-Fourier filter to obtain a lateral resolution equivalent to spherical harmonic degree $\ell=20$. Finally, to

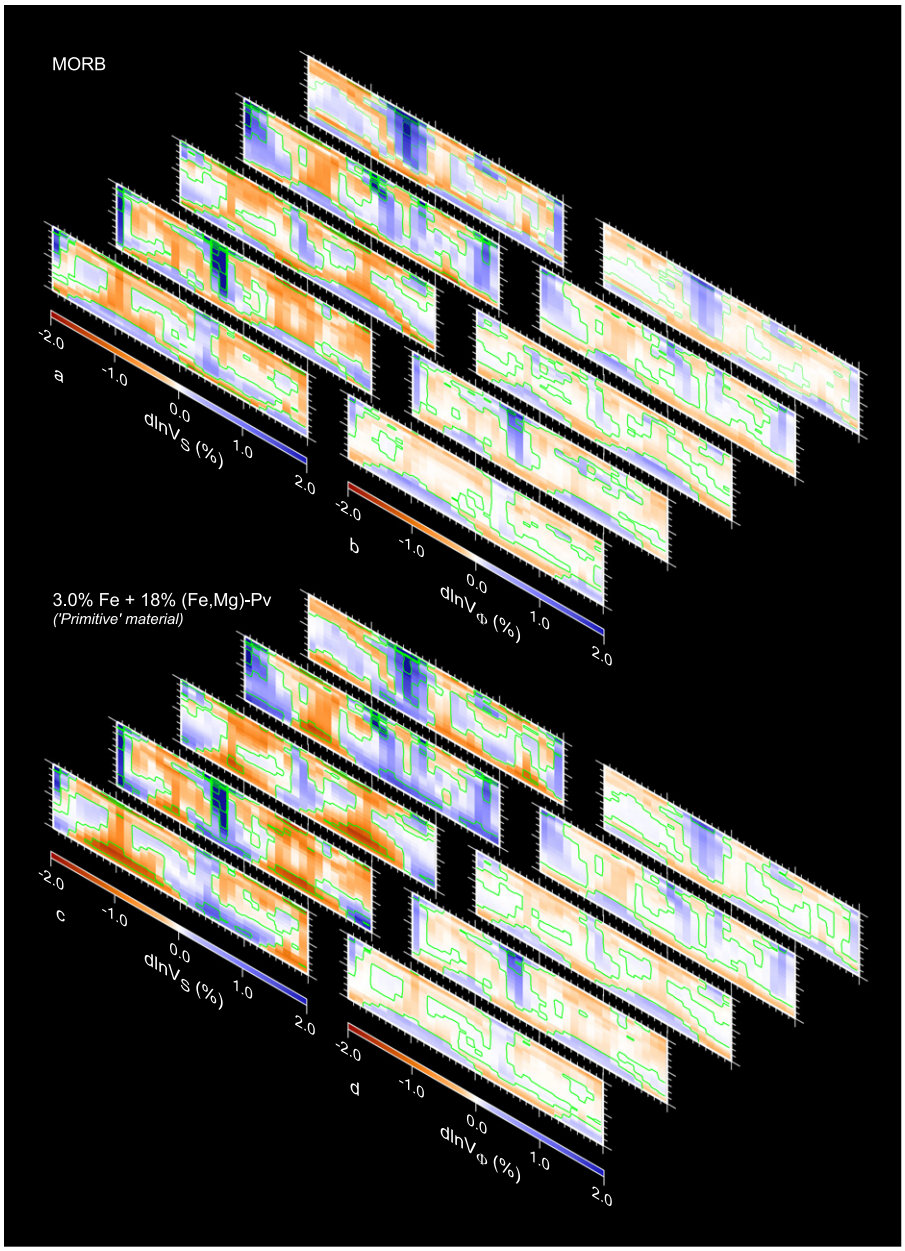

Fig. 5. Relative shear-wave ($d\ln V_S$) and bulk-sound ($d\ln V_\Phi$) velocity anomalies predicted by thermo-chemical convection. Represented anomalies are average in a collection of models obtained by varying seismic sensitivities according to their distribution, and the super-adiabatic temperature jump in the range 2000–3000 K. Vertical and lateral resolution are degraded to those of seismic tomography. Each of the 5 maps in each panel represents a vertical slice of the seismic velocity anomalies at fixed coordinates along the y-axis (see orientation on Fig. 4) of the box. Two types of chemical heterogeneities are considered, MORB with $dX_{MORB}=1$ in Eq. (3) (top), and material enriched (compared to pyrolitic mantle) in iron and (Mg,Fe)-perovskite by 3% and 18%, respectively (bottom).

model possible uncertainties in the observed seismic tomography, we added random noise following a Gaussian distribution with standard deviation equal to 20% of the unperturbed anomalies.

Fig. 5 displays the average in a collection of reconstructed $d\ln V_S$ and $d\ln V_\Phi$ obtained by varying seismic sensitivities according to their distribution and the super-adiabatic temperature jump in the range 2000–3000 K. The RMS of $d\ln V_S$ and $d\ln V_\Phi$ in the lowermost three layers, and the RMS of the uncertainties in $d\ln V_S$ and $d\ln V_\Phi$ (taken as one standard deviation around the average value) are listed in Table 2. Thermo-chemical reservoirs clearly have different seismic signatures depending on their assumed composition. If they consist of MORB, thermo-chemical reservoirs appear faster than average for both V_S and V_Φ, in contradiction with seismic tomography (Ishii and Tromp, 1999; Masters et al., 2000; Trampert et al., 2004). Furthermore, the RMS in average $d\ln V_S$ is slightly too low compared to that of SB10L18 (Table 2). By contrast, if they consist of material enriched in iron and perovskite, thermo-chemical reservoirs appear slower than average for V_S and faster for V_Φ, with RMS in $d\ln V_S$ and $d\ln V_\Phi$ in good agreement with observed ones (Masters et al., 2000). The RMS of uncertainties in reconstructed anomalies (Table 2) indicates that these signatures are robust features.

Table 2
RMS of average (denoted $\langle x \rangle$) and uncertainties (denoted σ_x) in a collection of randomly chosen models of relative shear-wave ($d\ln V_S$) and bulk-sound ($d\ln V_\Phi$) velocity anomalies at the bottom of the system. For comparison, RMS from SB10L18 (Masters et al., 2000) are also listed.

Quantity	Depth (km)	MORB		1.5% Fe+9.0% *Pv*		SB10L18
		$\langle x \rangle$	σ_x	$\langle x \rangle$	σ_x	
$d\ln V_S$ (%)	2300–2520	0.45	0.28	0.78	0.19	0.64
	2520–2700	0.51	0.38	1.02	0.25	0.79
	2700–2880	0.73	0.36	0.80	0.21	1.02
$d\ln V_\Phi$ (%)	2300–2520	0.28	0.21	0.15	0.10	0.27
	2520–2700	0.32	0.28	0.21	0.14	0.29
	2700–2880	0.27	0.26	0.25	0.12	0.37

4. Influence of the post-perovskite phase

The seismic sensitivities to post-perovskite indicate that V_S increases with increasing fraction of post-perovskite, and that V_Φ remains unchanged (Figure S6). Post-perovskite is thus unlikely to explain LLVSP, since it would result in positive $d\ln V_S$. The most recent models of probabilistic tomography (Mosca et al., 2012) reach a similar conclusion. One may point out that if LLVSP are hotter than average, post-perovskite may be a good explanation

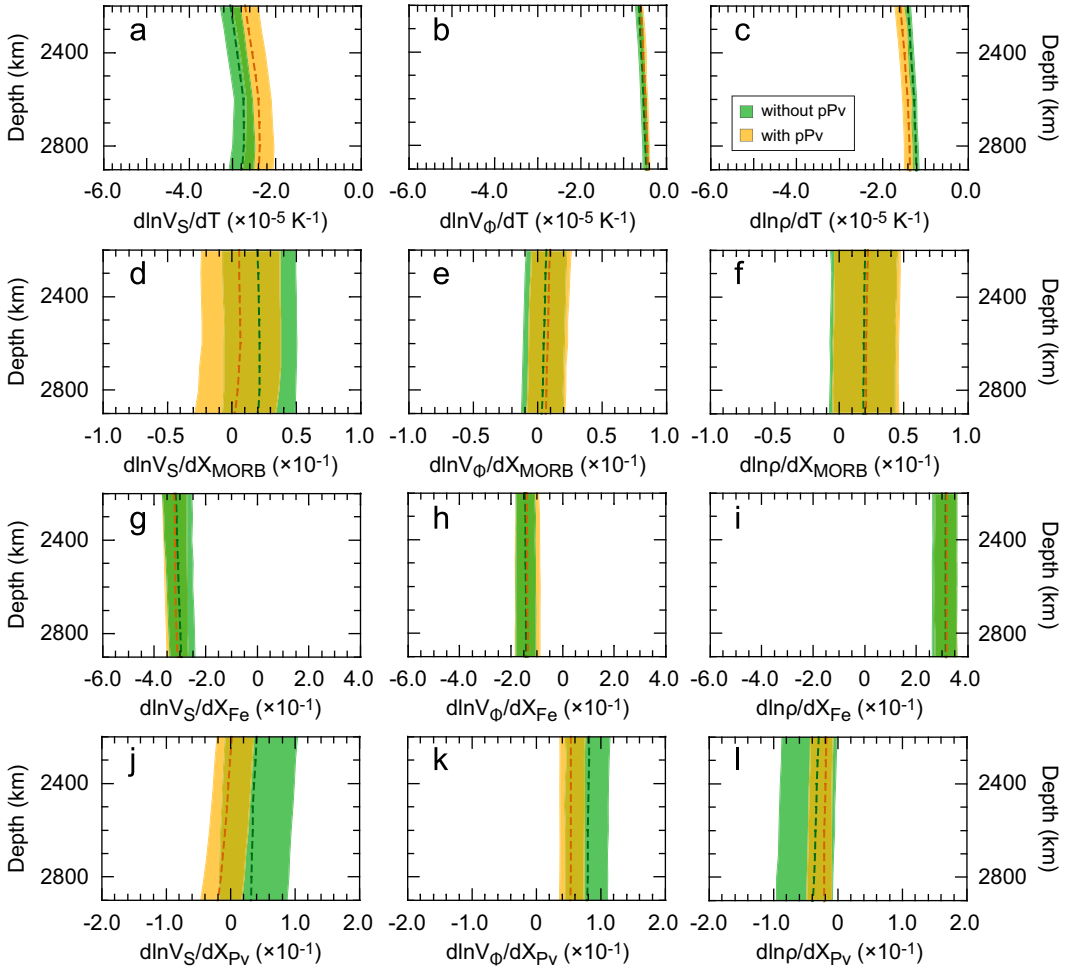

Fig. 6. Effect of the presence of post-perovskite on seismic sensitivities. Plots show sensitivities of shear-wave velocity (left column), bulk-sound velocity (middle column), and density (right column) to temperature (top row), MORB (2nd row), iron (3rd row), and (Mg,Fe)-perovskite (bottom row). Sensitivities are calculated assuming that post-perovskite is either absent (green areas) or present (orange areas) in the range 2200–2900 km. For each sensitivity, the coloured area encompasses the 0.15 to 0.85 quartiles (i.e., 70% of the explored sensitivities lie within this area), and the thick dashed curves denote the median value (i.e., 50% of the explored sensitivities lie on each side of this line).

to LLVSP. However, if LLVSP are too hot, they would be outside the stability field of post-perovskite.

Although it cannot explain LLVSP alone, post-perovskite slightly modifies the seismic sensitivities and may have a small influence on the interpretation of seismic tomography. Fig. 6 compares sensitivities obtained with (orange areas) and without (green areas) post-perovskite in the depth range 2200–2900 km. Overall, the presence of post-perovskite has only small to moderate effects on seismic sensitivities. Importantly, the relative roles of temperature and chemical compounds remain unchanged. In particular, excess in iron decreases V_S and increases V_Φ, whereas MORB increases both V_S and V_Φ, whether post-perovskite is present or not. Note that sensitivities to iron remain mostly unchanged (Fig. 6, plots g to i). The largest discrepancies are for sensitivities of V_S to temperature, MORB, and perovskite, and sensitivities of V_Φ to perovskite. Sensitivities of V_S to temperature are slightly smaller in amplitude when post-perovskite is present (Fig. 6, plot a), i.e. the signature of temperature is slightly attenuated. Furthermore, if post-perovskite is present, the sensitivity of V_S to MORB spans around the origin with a median value close to zero (Fig. 6, plot d). Consequently the presence of MORB is unlikely to result in large V_S-anomalies, although it is easier to generate negative V_S-anomalies. Another substantial change is that the sensitivity of V_Φ to perovskite is smaller (Fig. 6, plot k). Inducing moderate (0 to 1.0%) V_Φ-anomalies would thus require a larger fraction of perovskite and/or smaller temperature. To quantify the influence of these changes on the interpretation of seismic tomography, we calculated histograms of the distributions in $d\ln V_S$ and $d\ln V_\Phi$ at various temperatures (Fig. 7), and combined likelihood that $-3.0\% \le d\ln V_S \le -1.0\%$ and $0.0 \le d\ln V_\Phi \le 1.0\%$ (Fig. 3b), assuming that post-perovskite is present. Again, Figs. 3b and 7 suggest that MORB is unlikely to explain simultaneously low V_S and high V_Φ. For a temperature excess around 500 K, both $d\ln V_S$ and $d\ln V_\Phi$ are too small in amplitude (Fig. 7, plot c), and the likelihood that $-3.0\% \le d\ln V_S \le -1.0\%$ and $0.0 \le d\ln V_\Phi \le 1.0\%$ peaks around 0.1 (Fig. 3b). Note that compared to the case where post-perovskite was neglected (Fig. 3a), the maximum of likelihood has shifted to lower temperatrure anomalies, around 1000 K. This value is however still high compared to those estimated by excess temperature in plumes. By contrast, material enriched in iron by 1.5% and in perovskite by 9% explains low V_S and high V_Φ with likelihood up to 0.65. Again, compared to the case where post-perovskite was neglected, the excess temperatures required to explain low V_S and high V_Φ are smaller, in the range 200–500 K, which is still consistent with excess temperatures in plumes.

Finally, we considered the possibility that LLVSP consist of hot MORB entirely surrounded by post-perovskite. For this, we calculated an additional set of seismic sensitivities assuming a reference model in which all the non-MORB material is in the post-perovskite phase (Fig. 8). Compared to the case with no post-perovskite (Fig. 1), the sensitivity of V_S to MORB in the lowermost mantle is slightly negative (although it is spreading around zero within error bars), and the sensitivity of V_Φ is still positive, but

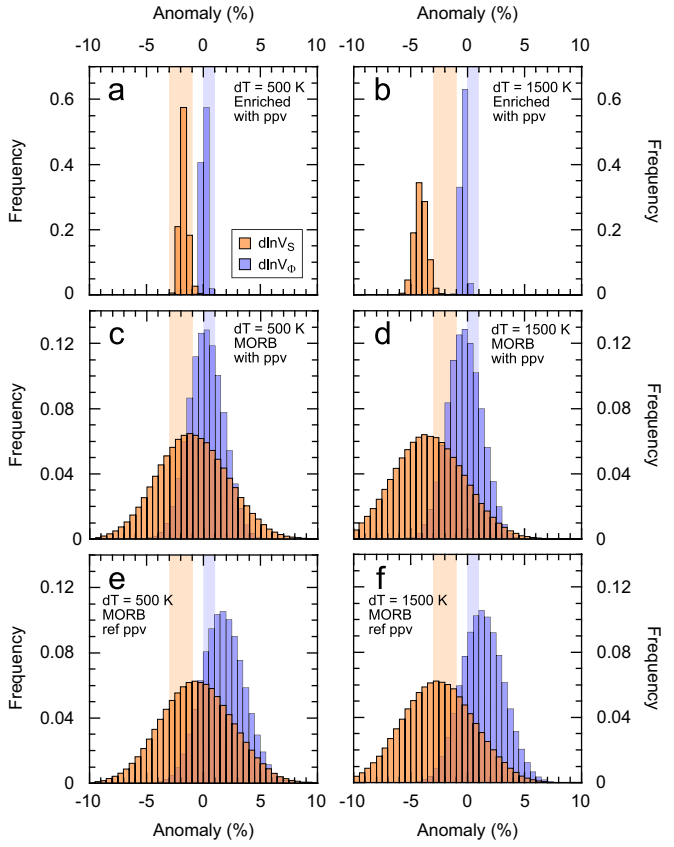

Fig. 7. Frequency histograms of shear-wave velocity (orange), and bulk sound velocity (blue) anomalies for material enriched in iron and (Mg,Fe)-perovskite with post-perovskite in the reference composition (top row), high pressure MORB with post-perovskite in the reference composition (middle row), and high pressure MORB surrounded by post-perovskite (bottom row). Two values of the excess temperature are considered, $dT = 500$ K (left), and $dT = 1500$ K (right). Shaded vertical bands indicate typical values for LLVSP observed from seismic tomography. Calculations are made in the layer 2700–2880 km, corresponding to the lowermost layer of tomographic model SB10L18 (Masters et al., 2000).

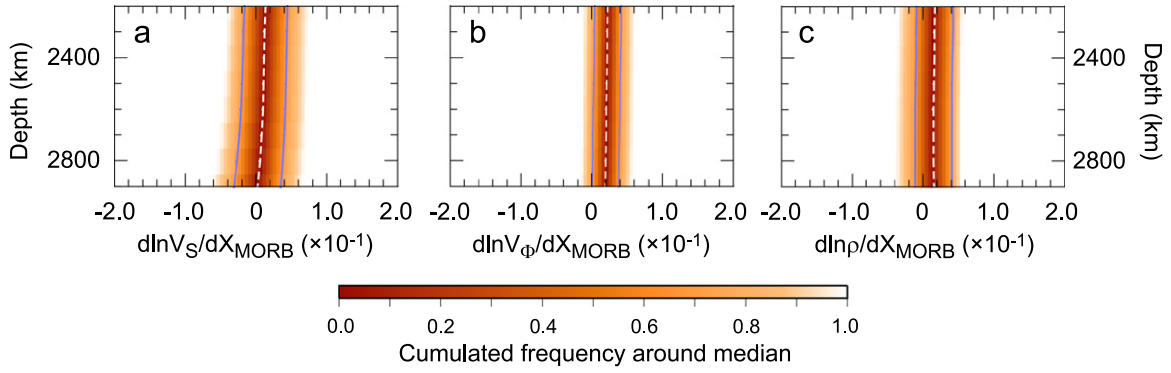

Fig. 8. Sensitivities of shear-wave velocity (left), bulk-sound velocity (middle), and density (right) to the volume fraction of MORB in the depth range 2200–2900 km, and assuming that all the non-MORB material is in the post-perovskite phase. The color code and curves description are similar to those in Fig. 1.

larger. As a consequence, for temperature excess in the range 500–1000 K, the $d\ln V_S$ induced by MORB are too small in amplitude, around -0.5%, and the $d\ln V_\Phi$ are too high, around 2.0% (Fig. 7, plots e and f). Furthermore, the induced $d\ln V_P$ are positive, in contradiction with the observed ones (Masters et al., 2000). For temperature excess around 1500 K, $d\ln V_\Phi$ is smaller in amplitude but still too large to explain the observed values, and $d\ln V_S$ is now slightly too large in amplitude.

Overall, the additional tests we performed indicate that the presence of post-perovskite in the lowermost mantle would not alter our main conclusions, i.e. LLVSP are better explained by material enriched in iron and silicate (the latter being in the form of perovskite), than by high pressure MORB, and rather consist of material enriched in iron and silicate (in the form of perovskite).

5. Concluding discussion

The seismic signatures we calculated clearly show that the chemical component in LLVSP is unlikely to consist of high-pressure MORB, but rather of a material enriched in iron and perovskite. A remaining question concerns the origin of such reservoirs. LLVSP may have been stable for at least 200 Ma (Torsvik et al., 2008; Dziewonski et al., 2010), and models of thermo-chemical convection (Deschamps and Tackley, 2008, 2009) indicate that thermo-chemical structures can be maintained over periods comparable to the age of the Earth. A possible hypothesis is that LLVSP result from the partial differentiation of the mantle early in the Earth's history (Solomatov and Stevenson, 1993; Labrosse et al., 2007; Lee et al., 2010), and subsequent interaction with mantle convection. Interestingly, recent mineral physics experiments (Nomura et al., 2011) predict that a primitive reservoir resulting from the crystallization of a basal magma ocean would be richer in iron. A primitive nature for LLVSP is also supported by geochemical observations. Enstatite chondrite models of Earth's composition (Javoy et al., 2010) lead to an Earth's lower mantle enriched in iron and silicate. In addition, the specific signatures of Ocean Island Basalts (OIBs) in rare gases and trace elements suggest the presence of reservoirs of undegassed material in the deep mantle (e.g., Farley et al., 1992; Hofmann, 1997; Stuart et al., 2003). Because they are sampled by OIB, these reservoirs are not strictly isolated, and small amounts of primitive material are entrained towards the surface. Recent numerical models (Deschamps et al., 2011) showed that the entrainment of dense material by plumes is less than 10%, in agreement with geochemical estimates (Allègre and Moreira, 2004). Finally, it is worth noting that the Fe/Mn ratio in Hawaiian lavas indicates that the source region of the Hawaiian plume, which may be located in the lowermost mantle, is enriched in iron (Humayun et al., 2004).

The enrichment in iron and (Mg,Fe)-perovskite needed to fit seismic observation, respectively around 3.0% and 18%, differ substantially from a regular pyrolitic composition. We checked that such compositions are stable at lower mantle temperatures and pressures using Perple_X (Conolly, 2005), which determines the most stable mineralogical composition at a prescribed composition, temperature, and oxides composition by minimizing the Gibbs free energy. Assuming volume fractions of FeO, MgO, and SiO_2 in pyrolite of 6%, 50%, and 40% (Ringwood, 1982), the volume fraction of (Mg,Fe)-perovskite at a depth of 2800 km and a temperature of 2500 K is around 70%. Figure S7 shows the phase diagram of material enriched in iron (FeO) by 3.0% and silicate (SiO_2) at same depth and temperature. We varied the fraction of SiO_2 in the range 40–50% (the fraction of MgO varying accordingly in the range 50–40%). For volume fractions of SiO_2 in the range 44–47%, the volume fraction of perovskite is larger than that in pyrolite by more than 18%, indicating that the combined enrichment in iron and perovskite required to explain seismic tomography is mineralogically viable at deep mantle conditions. For fractions of SiO_2 larger than 47%, some perovskite is replaced with free SiO_2 (seifertite), but the sum of the volume fraction of perovskite and free SiO_2 remains constant at around 92%. Because the seismic sensitivities to free SiO_2 are comparable to those of perovskite (Figure S5), such change would be difficult to detect with tomography. More importantly, it does not alter our main conclusion that LLVSP are well explained by a combined enrichment in iron and silicate, most of the silicate being included in the perovskite phase.

Our results do not mean that recycled MORB is not present at the bottom of the mantle. Tomographic images of slabs in the lower mantle (e.g., van der Hilst et al., 1997) clearly indicate that MORB may reach the lowermost mantle. However, this MORB would be distinct from the LLVSP, and its seismic signature would consist of positive anomalies in both V_S and V_Φ. The combination of primitive and recycled chemical heterogeneities at a global scale, and the presence of post-perovskite locally, may produce more complex seismic and geochemical signatures, including a substantial de-correlation between density and seismic velocity anomalies (keeping in mind that part of the observed de-correlation can be accounted for by vertical averaging), and a full description of the large scattering of the Helium isotopic ratio observed in OIB. Post-perovskite alone is unlikely to explain LLVSP, but may slightly modify the thermo-chemical interpretation of seismic tomography (Section 4). To fully explain geophysical and geochemical constraints, future models of thermo-chemical convection should thus include two chemical sources, recycled crust and primitive reservoirs, and the post-perovskite phase.

Acknowledgments

We are grateful to two anonymous colleagues for their comments and reviews that helped to improve a first version of this article. This research was initiated as FD was in ETH, and it was partly supported by the National Science Council of Taiwan (NSC grant 101-2116-M-001-001-MY3) and the German Research Foundation (DFG grant TH1530/5-1). Models of thermo-chemical convection were calculated on the ETH's Linux cluster Brutus.

Appendix A. Supporting information

Supplementary data associated with this article can be found in the online version at http://dx.doi.org/10.1016/j.epsl.2012.07.012.

References

Albers, M., Christensen, U.R., 1996. The excess temperature of plumes rising from the core-mantle boundary. Geophys. Res. Lett. 23, 3567–3570.
Allègre, C.J., Moreira, M., 2004. Rare gas systematic and the origin of oceanic islands: the key role of entrainment at the 670 km boundary layer. Earth Planet. Sci. Lett. 228, 85–92.
Brodholt, J.P., Helffrich, G., Trampert, J., 2007. Chemical versus thermal heterogeneity in the lower mantle: The most likely role of anelasticity. Earth Planet. Sci. Lett. 262, 429–437.
Bunge, H.-P., 2005. Low plume excess temperature and high core heat flux inferred from non-adiabatic geotherms in internally heated mantle circulation models. Phys. Earth Planet. Inter. 153, 3–10.
Campbell, I.H., Griffiths, R.W., 1990. Implications of mantle plume structure for the evolution of flood basalts. Earth Planet. Sci. Lett. 99, 79–93.
Christensen, U.R., Hofmann, A.W., 1994. Segregation of subducted oceanic crust in the convecting mantle. J. Geophys. Res. 99, 19867–19884.
Cobden, L., Goes, S., Ravenna, M., Styles, E., Cammarano, F., Gallagher, K., Connolly, J.A.D., 2009. Thermochemical interpretation of 1-D seismic data for the lower mantle: The significance of nonadiabatic thermal gradients and compositional heterogeneity. J. Geophysical Res. 114, B11309.

Cobden, L. Mosca, I., Trampert, J. Ritsema, J., Stixrude, L., Lithgow-Bertelloni, C., 2012. On the likelihood of post-perovskite at the core-mantle boundary: a statistical interpretation of seismological observations. (Submitted for publication).

Conolly, J.A.D., 2005. Computation of phase equilibria by linear programming: a tool for geodynamic modeling and its application to subduction zone decarbonisation. Earth Planet. Sci. Lett. 236, 524–541.

Davaille, 1999. Simultaneous generation of hotspots and superswells by convection in a heterogeneous planetary mantle. Nature 402, 756–760.

Deschamps, F., Trampert, J., 2003. Mantle tomography and its relation to temperature and composition. Phys. Earth Planet. Inter. 140, 277–291.

Deschamps, F., Tackley, P.J., 2008. Exploring the model space of thermo-chemical convection I – Principles and influence of the rheological parameters. Phys. Earth Planet. Inter. 171, 357–373.

Deschamps, F., Tackley, P.J., 2009. Searching for models of thermo-chemical convection that explain probabilistic tomography. II. Influence of physical and compositional parameters parameters. Phys. Earth Planet. Inter. 176, 1–18.

Deschamps, F., Kaminski, E., Tackley, P.J., 2011. A deep mantle origin for the primitive signature of Ocean Island Basalt. Nature Geosci. 4, 879–882.

Dziewonski, A.M., Lekic, V., Romanowicz, B., 2010. Mantle anchor structure: an argument for bottom up tectonics. Earth Planet. Sci. Lett. 299, 69–79.

Farley, K.A., Natland, J.H., Craig, H., 1992. Binary mixing of enriched and undegassed (primitive?) mantle components (He, Sr, Nd, Pb) in Samoan lavas. Earth Planet. Sci. Lett. 111, 183–199.

Farnetani, C.G., 1997. Excess temperature of mantle plumes: the role of chemical stratification across D. Geophys. Res. Lett. 24, 1583–1586.

Hirose, K., Takafuji, N., Sata, N., Ohishi, Y., 2005. Phase transition and density of subducted MORB crust in the lower mantle. Earth Planet Sci. Lett. 237, 239–251.

Hofmann, A.W., 1997. Mantle geochemistry: the message from oceanic volcanism. Nature 385, 219–229.

Hofmann, A.W., 1998. Chemical differentiation of the Earth – the relationship between mantle, continental crust and oceanic crust. Earth Planet. Sci. Lett. 90, 297–314.

Humayun, M., Qin, L., Norman, N.D., 2004. Geochemical evidence for excess iron in the Mantle beneath Hawaii. Science 306, 91–94.

Irifune, T., Ringwood, A.E., 1993. Phase transformations in subducted oceanic crust and buoyancy relationships at depths of 600–800 km in the mantle. Earth Planet. Sci. Lett 117, 101–110.

Ishii, M., Tromp, J., 1999. Normal-mode and free-air gravity constraints on lateral variations in velocity and density of Earth's mantle. Science 285, 1231–1236.

Javoy, M., Kaminski, E., Guyot, F., Andrault, D., Sanloup, C., Moreira, M., Labrosse, S., Jambon, A., Agrinier, P., Davaille, A., Jaupart, C., 2010. The chemical composition of the Earth: Enstatite chondrite model. Earth Planet. Sci. Lett. 293, 259–268.

Kiefer, B., Stixrude, L., Wentzcovitch, R.M., 2002. Elasticity of $(Mg,Fe)SiO_3$ perovskite at high pressures. Geophys. Res. Lett. 29 , http://dx.doi.org/10.1029/2002GL014683.

Kung, J., Li, B., Weidner, D.J., Zhang, J., Liebermann, R.C., 2002. Elasticity of$(Mg_{0.83},Fe_{0.17})$ O ferropericlase at high pressure: ultrasonic measurements in conjunction with X-radiation techniques. Earth Planet. Sci. Lett. 203, 557–566.

Labrosse, S., Hernlund, J.W., Coltice, N., 2007. A crystallizing dense magma ocean et the base of the Earth's mantle. Nature 450, 866–869.

Le Bars, M., Davaille, A., 2004. Whole layer convection in a homogeneous planetary mantle. J. Geophys. Res. 109 , http://dx.doi.org/10.1029/2003JB002617.

Lee, C.-T., Luffi, P., Hoink, T., Li, J., Dasgupta, R., Hernlund, J., 2010. Upside-down differentiation and generation of a 'primordial' lower mantle. Nature 463, 930–933.

Leng, W., Zhong, S., 2008. Controls on plume heat flux and plume excess temperature. J. Geophys. Res. 113 , http://dx.doi.org/10.1029/02007JB005155.

Li, X.-D., Romanowicz, B., 1996. Global mantle shear velocity model developed using nonlinear asymptotic coupling theory. J. Geophys. Res. 101, 22245–22272.

Machetel, P., Weber, P., 1991. Intermittent layered convection in a model mantle with an endothermic phase change at 670 km. Nature 350, 55–57.

Masters, G., Laske, G., Bolton, H., Dziewonski, A.M., 2000. The relative behavior of shear velocity, bulk sound speed, and compressional velocity in the mantle: implicationfor thermal and chemical structure. In: Karato, S.-I., et al. (Eds.), Earth's deep interior: mineral physics and tomography from the atomic to the global scale. Geophysical Monograph Ser. 117. American Geophysical Union, Washington, DC, pp. 63–87.

McNamara, A.K., Zhong, S., 2004. Thermochemical structures within a spherical mantle. J. Geophys. Res. 109 , http://dx.doi.org/10.1029/2003JB002847.

Mittelstaedt, E., Tackley, P.J., 2005. Plume heat flow is much less than CMB heat flow. Earth Planet. Sci. Lett. 241, 202–210.

Mosca, I., Cobden, L., Deuss, A., Ritsema, J., Trampert, J., 2012. Seismic and mineralogical structures of the lower mantle from probabilistic tomography. J. Geophys. Res., 117, , http://dx.doi.org/10.1029/2011JB008851.

Nakagawa, T., Tackley, P.J., Deschamps, F., Connolly, J.A.D., 2010. The influence of MORB and harzburgite composition on thermo-chemical mantle convection in a 3D Spherical shell with self-consistently calculated mineral physics. Earth Planet. Sci. Lett 296, 403–412.

Nomura, R., Ozawa, H., Tateno, S., Hirose, K., Hernlund, J., Muto, S., Ishii, H., Hiraoka, N., 2011. Spin crossover and iron-rich silicate melt in the Earth's deep mantle. Nature 473, 199–203.

Ono, S., Ito, E., Katsura, T., 2001. Mineralogy of subducted basaltic crust (MORB) from 25 to 37 GPa, and chemical heterogeneity of the lower mantle. Earth Planet. Sci. Lett. 190, 57–63.

Ono, S., Ohishi, Y., Isshiki, M., Watanuki, T., 2005. In situ X-ray observations of phase assemblages in peridotite and basalt compositions at lower mantle conditions: Implications for density of subducted oceanic plate. J. Geophys. Res. 110, B02208.

Parmentier, E.M., Sotin, C., Travis, B.J., 1994. Turbulent 3-D thermal convection in an infinite Prandtl number, volumetrically heated fluid - Implications for mantle dynamics. Geophys. J. Int. 116, 241–251.

Perrillat, J., Ricolleau, A., Daniel, I., Fiquet, G., Mezouar, M., Guignot, N., Cardon, H., 2006. Phase transformations of subducted basaltic crust in the upmost lower mantle. Phys. Earth Planet. Inter 157, 139–149.

Ricard, Y., Mattern, E., Matas, J., 2005. Synthetic tomographic images of slabs from mineral physics. In: van der Hilst, R.D., et al. (Eds.), Earth's deep mantle: Structure, composition and evolution. Geophysical Monograph Ser. 160. American Geophysical Union, Washington, DC, pp. 285–302.

Ricolleau, A., Perrillat, J., Fiquet, G., Daniel, I., Matas, J., Addad, A., Menguy, N., Cardon, H., Mezouar, M., Guignot, N., 2010. Phase relations and equation of state of a natural MORB: Implications for the density profile of subducted oceanic crust in the Earth's lower mantle. J. Geophys. Res. 115, B08202.

Ringwood, A., 1982. Phase transformations and differentiation in subducted lithosphere: implications for mantle dynamics, basalt petrogenesis, and crustal evolution. J. Geol. 90, 611–642.

Solomatov, V.S., Stevenson, D.J., 1993. Suspension in convective layers and style of differentiation of a terrestrial magma ocean. J. Geophys. Res. 98, 5375–5390.

Stixrude, L., Lithgow-Bertelloni, C., 2005. Thermodynamics of mantle minerals – I. Physical properties. Geophys. J. Int. 162, 610–632.

Stixrude, L., Lithgow-Bertelloni, C., 2011. Thermodynamics of mantle minerals – II. Phase equilibria. Geophys. J. Int. 184, 1180–1213.

Stuart, F.M., Lass-Evans, S., Fitton, J.G., Ellam, R.M., 2003. High $^3He/^4He$ ratios in picritic basalts from Baffin Island and the role of a mixed reservoir in mantle plumes. Nature 424, 57–59.

Su, W.-J., Woodward, R.L., Dziewonski, A.M., 1994. Degree 12 model of shear velocity heterogeneity in the mantle. J. Geophys. Res. 99, 6945–6980.

Tackley, P.J., 2002. Strong heterogeneity caused by deep mantle layering. Geochem. Geophys. Geosys. 3 , http://dx.doi.org/10.1029/2001GC000167.

Tackley, P.J., 2008. Modelling compressible mantle convection with large viscosity contrasts in a three-dimensional spherical shell using the yin-yang grid. Phys. Earth Planet. Inter 171, 7–18.

Tackley, P.J.. Dynamics and evolution of the deep mantle resulting from thermal, chemical, phase and melting effects. Earth Sci. Rev. in press.

Tan, E., Gurnis, M., 2007. Compressible thermo-chemical convection and application to the lower mantle. J. Geophys. Res., 112, , http://dx.doi.org/10.1029/2006JB004505.

Torsvik, T.H., Steinberger, B., Cocks, L.R.M., Burke, K., 2008. Longitude: linking Earth's ancient surface to its deep interior. Earth Planet. Sci. Lett. 276, 273–282.

Trampert, J., Vacher, P., Vlaar, N., 2001. Sensitivities of seismic velocities to temperature, pressure and composition in the lower mantle. Phys. Earth Planet. Inter 124, 255–267.

Trampert, J., Deschamps, F., Resovsky, J.S., Yuen, D.A., 2004. Probabilistic tomography maps significant chemical heterogeneities in the lower mantle. Science 306, 853–856.

van der Hilst, R.D., Widiyantoro, S., Engdahl, E.R., 1997. Evidence for deep mantle circulation from seismic tomography. Nature 386, 578–584.

van der Hilst, R.D., Kárason, H., 1999. Compositional heterogeneity in the bottom 1000 km of Earth's mantle: towards a hybrid convection model. Science 283, 1885–1888.

van Summeren, J.R.G., van den Berg, A.P., van der Hilst, R.D., 2010. Upwellings from a deep mantle reservoir filtered at the 660 km phase transition in thermo chemical convection models and implications for intra-plate volcanism. Phys. Earth Planet. Inter. 172, 210–224.